Bioinspired Electron Polarization of Nanozyme with Human Self-Generated Electric Field for Cancer Catalytic Therapy

Shuncheng Yao, Xinyang Zhao, Xueyu Wang, Tian Huang, Yiming Ding, Jiaming Zhang,

Zeyu Zhang, Zhong Lin Wang*, Linlin Li*

S. Yao, X. Zhao, X. Wang, X. Wang, T. Huang, Y. Ding, J. Zhang, Z. Zhang, Prof. Z. L. Wang, Prof. L. Li

Beijing Institute of Nanoenergy and Nanosystems

Chinese Academy of Sciences, Beijing 101400, P. R. China.

E-mail: zhong.wang@mse.gatech.edu, lilinlin@binn.cas.cn

S. Yao, J. Zhang, Prof. Z. L. Wang, Prof. L. Li

School of Nanoscience and Technology

University of Chinese Academy of Sciences, Beijing 101400, P. R. China.

T. Huang, Y. Ding, Z. Zhang, Prof. Z. L. Wang, Prof. L. Li

Center on Nanoenergy Research, Guangxi University, Nanning, 530004, China

Prof. Z. L. Wang

School of Materials Science and Engineering, Georgia Institute of Technology, Atlanta, GA 30332-0245, USA

ROS production efficiencies of the nanocatalysts is highly desired for cancer therapy, but currently the ROS generation efficiency is still far from defecting the tumors. Therefore, improving their ROS generation ability is highly desirable for cancer therapy. Herein, inspired by the electrostatic preorganization effect during the catalysis of natural protein enzymes, we developed a human self-driven catalysis-promoting system, TENG-CatSystem, to improve catalytic cancer therapy. TENG-CatSystem is mainly composed of three main elements: a human self-driven triboelectric nanogenerator (TENG) as the electric field stimulator to provide electric pulses with high biosafety, a nanozyme comprising a one-dimensional ferriporphyrin covalent organic framework coated on a carbon nanotube (COF-CNT) to generate ROS, and a COF-CNT-embedded conductive hydrogel that can be injected into the tumor tissues to increase local accumulation of COF-CNT and decrease the electrical impedances of tissues. Under the human self-generated electric field provided by the wearable TENG, the peroxidase-like activity of COF-CNT was four-fold higher than that without an electric field. Highly malignant 4T1 breast carcinoma in mice was significantly suppressed using TENG-CatSystem. The human self-driven TENG-CatSystem not only demonstrates high catalytic ROS generation efficiency for improved cancer therapy, but also offers a new therapeutic mode of self-driven at-home therapy.

1. Introduction

Producing excessive reactive oxygen species (ROS) in local tumor tissues to induce lethal oxidative damage is a highly specific and efficient pathway for cancer therapy and is called dynamic therapy[1]. Among different dynamic therapies, nanocatalytic therapy, also termed nanozyme catalysis, involves the production of ROS via the catalysis of specific endogenous molecules in the tumor microenvironment (TME) by biocompatible nanozymes[2]. Nevertheless, the relatively low catalytic efficiencies and inferior catalytic kinetics of current nanozymes in strict TMEs are critical obstacles for effective cancer therapy. Once ROS generation is inadequate, due to the upregulated antioxidant defense system of tumor cells, the cells may escape or recover from oxidative damage, which may lead to tumor proliferation, recurrence, and metastasis[3]. Recently, to activate the current nanozymes and improve their catalytic activities and therapeutic outcomes, different external stimulators have been locally used to improve the catalytic efficiency, including near-infrared light[4], ultrasound[5], magnetic field[6], microwave[7], and electricity[8].

With regard to using electricity as a stimulator, natural protein enzymes are considered to have strong and permanent electrostatic fields in their active sites, which are believed to be the major factor responsible for the binding of these enzymes with substrates and subsequent catalytic reactions, namely the electrostatic preorganization effect[9]. Accordingly, researchers have applied an external electric field to remodel the internal electrostatic field of enzymes to control the reactivities and selectivities of catalytic reactions[10]. For instance, in the cases of heme-Fe enzymes, the external electric field can change their electronic structures,

3

localizations of unpaired electrons, and locations of radical sites[11]. With respect to the application of electricity in cancer therapy, previously, electric field has been employed in the clinic for electrochemotherapy to promote the transport of cytotoxic drugs across the plasma membrane via electroporation[8a]. Compared to other external stimulators, electricity has a broad actuation field to cover the entire tumor volume, thereby avoiding the possibility of escape of a small number of tumor cells from damage and the risk of tumor relapse. However, the applications of existing electric field-based therapies are mainly hindered by the risks associated with the use of strong electric fields and high voltages and the inconvenience of bulky external equipment. Moreover, to date, only a few studies have investigated the promotion effect of electric field on nanocatalysis for *in vivo* cancer therapy[8].

Triboelectric nanogenerators (TENGs) can convert mechanical energy into electricity based on contact electrification and electrostatic induction[12]. Since their invention, many TENGs have been developed for various applications. Particularly, TENGs that can convert human body movements, such as heartbeat, breathing, and daily movements, into electrical signals have been used in unique self-powered biomedical applications including biosensing[13], drug delivery[14], and tissue repair[15]. In addition to the unique self-generation possibility, the electric signals from TENGs have additional advantages for *in vivo* biomedical applications compared with the traditional electric stimulators. TENGs with high voltages and low current outputs are highly biosafe for *in vivo* applications. Moreover, TENGs with frequencies of a few Hz can be directly applied without external energy transmitters to facilitate the therapy. To date, no studies have been reported on the application of self-driven catalysis in biomedical field. With an expanding application of TENG-assisted catalysis in the energy and environmental fields [16], the development of a cancer therapeutic

system using a human self-generated electric field to promote nanozyme catalysis is expected, which may be a promising pathway to improve the catalytic activities of nanozymes.

Inspired by the electrostatic preorganization effect in natural enzymes, herein, we designed a self-driven TENG-stimulated therapeutic catalytic system (abbreviated as TENG-CatSystem). At first, we rationally fabricated a one-dimensional (1D) metal/covalent organic framework (COF) coated on a carbon nanotube (denoted as COF-CNT) as a prototypical example of an efficient nanozyme[17]. In COF-CNT, ferriporphyrin (TAPP-Fe) was used as a building module of COF, and 2,5-dihydroxyterephthalaldehyde (DHPA) was employed as the linker, forming imine bonds with TAPP-Fe (**Figure 1**A). TAPP-Fe has a molecular structure analogous to that of heme, in which atomically dispersed Fe as the catalytic active center is coordinated in the middle of the porphyrin ring. In TME, Fe can be completely exposed to catalyze the decomposition of H_2O_2 to form toxic hydroxyl radicals (·OH); that is, COF-CNT exhibits peroxidase (POD)-like activity. The 1D closed encircling π-conjugated structure of COF-CNT with a high π-electron delocalization and high electron transport facilitates the catalytic decomposition of H_2O_2. Thus, it provides an ideal platform for the rapid movement and separation of electrons under an external electric field. To enhance the accumulation of COF-CNT at the tumor site and improve the electron transport ability of COF-CNT under an electric field, COF-CNT was embedded in a poly(2,3-dihydrothieno-1,4-dioxin):poly(styrene sulfonate) conductive hydrogel (PEDOT:PSS), and the resulting hydrogel is denoted as PC hereinafter. PEDOT:PSS has good biocompatibility and excellent electronic conductivity[18]. PC was prepared through simply mixing COF-CNT, PEDOT:PSS using 4-dodecylbenzenesulfonic acid (DBSA) as a secondary dopant and surfactant. PC can be directly injected into tumor tissues to fix

COF-CNT and reduce the local electrical impedance. A self-driven wearable TENG that could be attached to the human forearm to generate electric pulses under motion was fabricated to afford an external electric field to be exerted on tumors.

2. Results and discussion

2.1. Synthesis of COF-CNT and PC

As observed in scanning electron microscopy (SEM) (Figure 1B) and high-resolution transmission electron microscopy (HR-TEM) images (Figure 1C), a nanolayer with a thickness of ~4.7 nm was coated on the outer surface of CNT. COF-CNT had a typical 1D core-shell nanotubular structure with an outer diameter of 26 ± 1 nm, wall thickness of ~12.3 nm, and inner diameter of ~5.6 nm. As noticed in the energy-dispersive X-ray spectroscopy elemental mapping images (Figure 1D), C, N, O, and Fe were evenly distributed in the nanotube. X-ray diffraction (XRD) pattern of COF-CNT demonstrated a strong diffraction peak at 18.3° corresponding to the (010) plane of COF (Figure 1E), consistent with the diffraction ring data (Inset of Figure 1C). X-ray photoelectron spectrum of COF-CNT indicated that COF-CNT contained both Fe^{2+} (714.3 eV) and Fe^{3+} (711.0 eV) (Figure 1F). The N 1s spectrum was deconvoluted into three peaks centered at approximately 400.4, 399.3, and 398.8 eV, which were attributed to C-N, N-H, and C=N groups in COF, respectively (Figure 1G), confirming the formation of imine bonds. The stretching peak of C=N at 1610 cm^{-1}, the peak of -NH_2 at 3332 cm^{-1}, and the disappearance of the C=O peak at 1693 cm^{-1} in the Fourier transform infrared (FTIR) spectrum of COF-CNT also proved the existence of imine bonds (Figure 1H).

During the construction of PC, when the concentration of DBSA reached the threshold value of 3 v/v%, spontaneous gelation occurred with physical crosslinking between PEDOT polymer chains. The porous structure of PC had no significant change when compared with PEDOT:PSS (Figure 1I), and the pore size was in the range of 9.3–37.3 μm. In the XRD pattern of PC (Figure 1E), the diffraction peak at 18.3° originating from COF-CNT was still observed. In the FTIR spectrum of PC, the C-S vibrational peak at 870 cm^{-1} confirmed the presence of PEDOT:PSS and the incorporation of COF-CNT into PEDOT:PSS. These results verify the successful incorporation of COF-CNT into PEDOT:PSS.

2.2. Fabrication and performance of the self-driven TENG

To employ the human self-generated electric field as a stimulator, we fabricated a biomechanical energy-driven interdigital electrode (IDE)-based TENG (**Figure** 2A). A conducting Cu foil electrode attached to an acrylic substrate was cut into parallel finger electrodes separated by small gaps. A polytetrafluoroethylene (PTFE) film attached to the surface of the human finger served as a friction layer. Schematic of one working cycle of the IDE-based TENG is depicted in Figure 2B. Briefly, when the positively charged PTFE film touches the first Cu finger electrode, positive and negative polarities are generated on the PTFE film and Cu electrode, respectively, via contact electrification. Negative charges accumulate at the Cu electrode to effectively screen the positive charge of the PTFE film. When the finger with the PTFE film moves along the Cu surface, the accumulated negative charges flow through the Cu electrode to produce an electric current. When the PTFE film reaches the top of the second Cu electrode, negative charges accumulate at this electrode to screen the positive charge of the PTFE film. When the PTFE film travels in the opposite

Accepted Article

direction along the Cu surface, the accumulated negative charges reversely flow through the Cu electrode. Consequently, the accumulated charges move back and forth to generate continuous alternating current peaks. When ten tandem Cu finger electrodes are used in the TENG, a cycle of finger friction movement can produce ten current peaks. The working principle of the TENG was confirmed via finite element simulation using COMSOL (Figure 2C). According to the simulation results, the PTFE film tends to induce a negative electrostatic field (or a negative charge) to contact the original Cu electrode and move away from it. When the PTFE film approaches or moves away from the Cu electrode, the electric potential difference accordingly changes. Under the action of the changing potential difference, free electrons flow and achieve an electrostatic equilibrium. During this process, an alternating current can be generated in the external circuit. Experimentally, the output performance of the IDE-based TENG was detected under the finger motion of a student volunteer. With finger friction at a frequency of approximately 3.5 Hz, the peak open-circuit voltage (V_{oc}) and short-circuit current (I_{sc}) reached 33 V and 1 µA (Figures 2D and E), respectively. With an increase in load resistance, the output current decreased and the output voltage accordingly increased (Figure 2F). The matched resistance of the TENG was 40.4 MΩ, under which the TENG produced a maximum power of 20.4 µW, corresponding to a power density of 1.46 mW m^{-2} (Figure 2G). After approximately 21,000 cycles of friction (within a period of approximately 300 s), the V_{oc} remained stable (V_{oc} = ~30 V) (Figure 2H), demonstrating the excellent stability of the TENG.

2.3. Mechanical properties of the conductive hydrogels

Mechanical properties of PEDOT:PSS and PC were evaluated. Storage modulus (G′) of PC was lower than the loss modulus (G″) when the shear stress increased over 50 Pa, indicating that the PC network was broken under this stress (Supplementary Figure 10). The stress in the case of PC was slightly lower than that for PEDOT:PSS (56 Pa). This was attributed to the change in polymer organization and increase in the pore size upon the incorporation of COF-CNT into the network of PEDOT:PSS[19]. The viscosities of both PC and PEDOT:PSS substantially decreased with an increase in shear rate from 0.1 to 10 s^{-1} (**Figure** 3A), implying that the hydrogels with tandem dynamic covalent bonds had suitable shear-thinning properties. PC was injectable, ensuring its *in vivo* biomedical applications (Supplementary Video 1). Moreover, rapid recovery of hydrogel strength following injection is important for *in vivo* applications. Thus, step-strain measurements were performed to examine the self-healing properties of the hydrogels at the alternating strains of 1 and 100% at room temperature; G′ of PC decreased to be smaller than G″ at the strain of 100% (Figure 3B), suggesting disruption of the hydrogel network at a high strain[20]. When the strain was changed to 1%, the G′ and G″ of PC completely recovered within a short time of 3 s. In comparison, the self-healing time of PEDOT:PSS was 2.3 s, demonstrating that the incorporation of COF-CNT slightly reduced the crosslinking degree of the hydrogel. Overall, these results confirm that PC was injectable and had self-healing properties, suitable for local intratumoral injection.

For the TENG-CatSystem, the PC was injected into the tumor tissue to decrease the local electrical impedance, which exhibited high electrical conductivity (Supplementary Video 2). Electrochemical impedance spectroscopy (EIS) verified that PC had higher conductivity and

electron transfer ability than those of PEDOT:PSS due to the high conductivity of the incorporated COF-CNT (Figure 3C). Thus, we separately injected 100 μL of both hydrogels into subcutaneous 4T1 tumors with sizes of ~300 mm^3 and analyzed the current under an external applied voltage of 30 V (Supplementary Figure 13). Results showed that compared with the passing current of intact tumor tissue (98.6 μA), the passing currents of tumor tissues injected with PC and PEDOT:PSS were 2726.7 and 1693.3 μA, which were 27.65- and 17.17-fold higher than that of the intact tumor tissue, respectively. This finding proved that the injection of a conductive hydrogel into tumor tissues can efficiently reduce the electrical impedance for improving outcome of electrical stimulation.

2.4. Performance and mechanism of TENG-CatSystem

Subsequently, we evaluated the catalytic activity of COF-CNT under the self-generated electric field. The effects of the electric field and PEDOT:PSS on the POD-like activity of COF-CNT were examined using the colorimetric substrate 3,3',5,5'-tetramethylbenzidine (TMB) (Figure 3D) and electron spin resonance (ESR) spectroscopy using 5, 5- dimethyl- 1- pyrroline N- oxide (DMPO) as a ·OH-trapping agent (Figure 3E). The pH value employed for detection was 6.5, which was similar to that of the TME. Catalytic activity of PEDOT:PSS with and without the electric field was almost negligible. Under the self-generated electric field, the POD-like activities of COF-CNT and PC were significantly improved. The Michaelis-Menten kinetic constant of PC under the self-generated electric field was calculated to be 3.2 mM, which was 4-fold higher than that of PC without the electric field (Table S2). PC showed voltage-, frequency-, and pH-dependent ·OH production (Figure 3F). With an increase in the voltage and frequency of the electric field and a decrease in pH, the generation of ·OH increased.

Cyclic voltammetry was used to investigate the catalytic reaction under simulated TME

conditions (pH: 6.5 and H_2O_2: 100 μM). With the addition of H_2O_2, the current for PC considerably increased at a bias voltage of -0.6 V (Figure 3G), which was ascribed to the oxidation–reduction of PC with H_2O_2[21]. In comparison, the current of PC at -0.6 V in the presence of H_2O_2 was 44-fold that of COF-CNT and 1.49-fold that of PC without H_2O_2.

To determine the reason for the high POD-like activity of COF-CNT under an electric field, an electrostatic two-dimensional simulation was conducted using COMSOL to calculate the polarization degree of the COF-CNT surface in an ideal environment. In the simulation, two extreme situations with COF-CNT parallel and perpendicular to the electric field lines were separately considered. Under an applied electricity of 30 V, electric polarization of COF-CNT as a dielectric increase, which further facilitates the separation of positive and negative charges (Figure 3H). The simulation results showed that charge polarization occurs on the surface of COF-CNT, and the polarization mode is ~23 C m^{-2}. This further accelerates the production and movement of electrons, thereby boosting the POD-like activity of COF-CNT[22]. The occurrence of polarization is not affected by the direction of COF-CNT in the electric field. Furthermore, the degree of surface polarization increases with an increase in the voltage of the electric field, which can be benefited from the self-driven TENG with a high voltage output. In another hand, compared with the case of COF-CNT in a non-conductive medium, PEDOT:PSS provided an excellent medium for the movement of electrons. These two factors codetermine the substantially high catalytic activity of TENG-CatSystem for the generation of toxic ·OH.

2.5. *In vitro* cancer therapy

Considering the high catalytic performance of TENG-CatSystem, the anticancer ability of TENG-CatSystem was investigated. After being co-incubated with PC for 2 h, the normal murine NIH-3T3 fibroblasts exhibited high cell viabilities of approximately 100%, indicating

high cytocompatibility of PC. The *in vitro* anticancer effect of TENG-CatSystem was evaluated on a murine mammary carcinoma cell line 4T1 with high malignancy. To simulate the *in vivo* situation and directly observe the changes in 4T1 cells during treatment, a transwell culture system with a 0.4 μm pore polyester membrane insert was employed. PC connected to the human finger-driven TENG via a pair of Cu wires was placed in the upper chamber of the transwell, and the cells were seeded at the bottom of the transwell chamber (**Figure** 4A). Interestingly, although the catalytic reaction occurred in the upper chamber of the transwell, the catalytically generated ·OH could be detected in the bottom chamber, confirming that ·OH directly interacted with and acted on the cancer cells (Supplementary Figure 23). Electric field stimulation was performed via the self-driven TENG for 3 min (a total of ~6480 electric pulses).

The cells were divided into the following six groups: cells without any treatment (control group), cells treated with PEDOT:PSS (PEDOT:PSS group), cells treated with electric field stimulation (E group), cells treated with PEDOT:PSS under electric field stimulation (PEDOT:PSS+E group), cells treated with PC without electric field stimulation (PC group), and cells treated with PC under self-generated electric field stimulation (PC+E group). Thereafter, 100 μM H_2O_2 was added to all the groups to simulate the overproduction of H_2O_2 in TME, which acted as the substrate of POD-like nanozyme. Consequently, for the PEDOT:PSS, E, and PEDOT:PSS+E groups, low cell killing abilities with cell viabilities >60% were observed (Figure 4B). The PC group demonstrated a cell viability of 54%. In contrast, in the case of the PC+E group, the cell viability significantly decreased to 24.8% (Figure 4B). Live/dead cell fluorescence staining (Figure 4C) and apoptosis analysis by flow cytometry via PI/Hoechst 33342 double staining (Figure 4D) also proved the abovementioned results. Based on the apoptosis analysis by flow cytometry, the early apoptotic and late

apoptotic/death cells in the PC group were 32.2 and 36.2%, respectively, whereas the early apoptotic and late apoptotic/death cells in the PC+E group were 12.2 and 72.4%, respectively, indicating that the electric field induced enhanced killing of cells (Figure 4D).

Intracellular ROS levels of the cells after different treatments were detected using 2′, 7′-dichlorodihydrofluorescein diacetate (DCFH-DA) as a ROS indicator. The cells in the PC group demonstrated high ROS levels (Figure 4E). Furthermore, the cells in the PC+E group showed the highest fluorescence, which was 2.4- and 24.6-fold higher when compared with those of the PC and control groups, respectively. In addition, flow cytometry analysis demonstrated similar results (Figure 4F), implying that electric field stimulation accelerated catalyzed production of toxic ROS and activated the elevation of intracellular ROS levels. Subsequently, oxidative damage to deoxyribonucleic acid (DNA), proteins, and lipids of the cells were investigated. The levels of 8-hydroxy-2′-deoxyguanosine (8-OHdG, a DNA oxidative damage biomarker), protein carbonyl (PCO, representing the protein oxidation level), and 4-hydroxynonenal (4-HNE, a lipid oxidative damage biomarker) in the cells of the PC+E group were 2.1-, 11.2-, and 1.62-fold higher than those in the cells of the control group, respectively; in contrast, the oxidative damage was almost negligible in the case of the E group (Figure 4H). As mitochondria are the main targeting subcellular organelles of ROS-induced cellular oxidative damage, we also detected changes in mitochondrial membrane potentials (MMPs) of the different groups using 5,5,6,6-tetrachloro 1,1,3,3-tetraethyl-imidacarbocyanine (JC-1) as a specific indicator. According to the changes in the red:green fluorescence ratio, in which red fluorescence originates from the J-aggregates representing high MMPs, and green fluorescence arises from the monomeric forms indicating low MMPs, the changes in MMPs can be detected. The cells in the control, PEDOT:PSS, E, PEDOT:PSS+E, and PC groups primarily showed red fluorescence, and their green

fluorescence signals could be nearly ignored (Figure 4I and Supplementary Figure 33). In contrast, the cells in the PC+E group demonstrated the highest green:red fluorescence ratio, which was 315-fold increase when compared with that of the cells in the control group (Figure 4I). This suggested that the cells in the PC+E group had the highest degree of mitochondrial oxidative damage.

Electroporation is a common technique used for introducing macromolecules and drugs into cells under a strong external electric field, which can increase the permeability of the plasma membrane. To distinguish the effect of electric field on COF-CNT from those of other possible factors, we observed the changes in the plasma membrane potentials of the various groups. During electric field stimulation for 180 s, the plasma membrane potentials of the cells in the E, PEDOT:PSS+E, and PC+E groups increased by 1.74-, 1.96-, and 2.14-fold as compared to that of the cells in the control group, respectively, implying enhanced membrane permeabilities for these groups (Figure 4J and Supplementary Figure 34). Moreover, after a further 1 h incubation of the cells, the plasma membrane potential almost returned to the initial level before stimulation, indicating that the electroporation-induced membrane permeability enhancement was transient (Figure 4J). Note that during all the cell staining experiments, including the live/dead cell fluorescence staining, apoptosis analysis by flow cytometry, and intracellular ROS detection, fluorescent probes were added after 1 h incubation of the cells post-E stimulation, which excluded the possibility of electroporation-induced entry of dyes into cells. By combining the abovementioned findings with the cell viability result (that is, the electric treatment had a slight cell killing effect of ~20%) (Figure 4c), it was deduced that for the E group, the electroporation effect did not induce lethal damage to the cells. Instead, the electroporation effect transiently increased the cell membrane permeability, which might facilitate the entry of catalytically generated ·OH

from PC into the cells, although not definitely determined. In summary, it was deduced that the increased cell membrane permeability for the PC+E group when compared with that of the E group was due to enhanced oxidative cellular damage, which was caused by the increased production of ROS from PC under the electric field.

Intracellular ROS levels are influenced by many cellular events such as cell membrane damage and changes in intracellular Ca^{2+} concentration ($[Ca^{2+}]_i$). Thus, we could not directly conclude that the intracellular ROS elevation was entirely induced by the entry of extracellularly generated ·OH into the cells. To further examine the possible mechanism of the effect of the electric field on cell activity, we also investigated changes in $[Ca^{2+}]_i$ during the experiment. Changes in $[Ca^{2+}]_i$ after different treatments were detected using Fluo-4 AM as the $[Ca^{2+}]_i$ indicator. During the treatments, Ca^{2+}-containing phosphate buffered saline (PBS) and Ca^{2+}-free Dulbecco's phosphate buffered saline (DPBS) were separately used as extracellular fluids. Results showed that after PC+E treatment of the cells in Ca^{2+}-containing PBS, $[Ca^{2+}]_i$ was 1.98-fold higher than that before this treatment. In contrast, when Ca^{2+}-free DPBS was used, $[Ca^{2+}]_i$ after PC+E treatment of the cells was only 1.3-fold higher than that before this treatment (Figure 4G). This implied that the increase in $[Ca^{2+}]_i$ was mainly caused by the influx of Ca^{2+} instead of the release of Ca^{2+} from the intracellular Ca^{2+} pool. In the case of the E group, although $[Ca^{2+}]_i$ increased, the intracellular ROS level demonstrated no considerable change when compared with that of the control group, as discussed earlier. These results together proved that mere Ca^{2+} influx did not significantly increase the intracellular ROS levels and subsequent cell death. We deduced that the catalytically generated ·OH under E stimulation might destroy the cytomembrane, inducing the passive entrance of Ca^{2+} into cells. Therefore, the $[Ca^{2+}]_i$ elevation might be not only contributed from the Ca^{2+} entered through transmembrane calcium channel, but also those through

passive diffusion. For the PC+E group, the destruction of the cytomembrane by catalytically generated ·OH might also enhance the passive entry of ·OH into the cells.

2.6. *In vivo* cancer therapy

Owing to the high *in vitro* biocompatibility and anticancer activity of TENG-CatSystem, *in vivo* cancer therapeutic effect of TENG-CatSystem was evaluated in 4T1 tumor-bearing BALB/c mice (**Figure** 5A). The tumor-bearing mice were divided into six groups (n=6): 1) Control group, 2) E group, 3) PEDOT:PSS group, 4) PEDOT:PSS+E group, 5) PC group, and 6) PC+E group (Figure 5B). The details of these groups are provided in the Experimental Section. For electric field stimulation, the human self-driven flexible TENG was attached to the forearm of the volunteer via fluorinated ethylene propylene (FEP) bonding and operated by the finger of the volunteer at a frequency of 3.5 Hz for 3 min for pulsed electric field stimulation (Supplementary Video 3). The electric field of the self-driven TENG was delivered to local tumor tissues via two Ag needle electrodes for moxibustion inserted into the two opposite sides of each tumor tissue (E = 6 V mm^{-1}). At the experimental terminal, the tumors of two out of the six mice in the PC+E group were completely eradicated and the growths of tumors in the other four mice were significantly inhibited after a single treatment (Figure 5C–G). In contrast, the growths of the tumors of all mice in the PC, E, and PEDOT:PSS+E groups were only partially inhibited. Tumor inhibition rates of the PC+E, PC, E, PEDOT:PSS+E, and PEDOT:PSS groups were 83.6, 32, 26.3, 27.4, and 2.6%, respectively. Further histopathological analyses, including hematoxylin and eosin (H&E) staining and Ki-67 immunohistochemistry, confirmed the inhibition of the growth of malignant cells. Experimental results showed that the malignant cells were partially restrained in the PC, E, and PEDOT:PSS+E groups and were almost invisible in the PC+E

group (Figure 5H). The excellent therapeutic effect of TENG-CatSystem can be mainly attributed to the improved POD-like activity of COF-CNT under the self-generated electric field.

3. Conclusion

In conclusion, herein, we designed and fabricated a self-driven catalysis-promoting system, TENG-CatSystem, to improve the catalytic cancer therapy. Compared to the traditional method of electrical stimulation, the wearable TENG as an electric field simulator has the advantages of self-driven ability to spare cumbersome electrical stimulator, high biosafety, less side effects, and flexible modulation. Inspired by heme-ion enzymes whose activity can be modulated by an external electric field, Fe-porphyrin with analogous structure was selected as the module to construct COF on CNT, which contains the inserted Fe as the POD-like catalytic active center. COF-CNT has extended π-conjugation and full electron delocalization, promoting the catalytic reaction, which is also susceptible to an external electric field. Injectable PEDOT:PSS efficiently decreased the electrical impedance of tumors for facilitating electric field stimulation. At an applied voltage of 30 V, the POD-like catalytic activity of COF-CNT was ~4-fold higher as compared to that without the applied voltage, and with an increase in the applied voltage, the catalytic activity of COF-CNT further increased, which was favorable for TENG with a wide voltage range. During the course of therapy, the electric field promoted the acquisition and loss of electrons and accelerated the catalytic reaction, which was primarily due to the accelerated separation of positive and negative charges near the active centers. Via these efforts, improved cancer suppression was successfully realized *in vitro* and *in vivo* using TENG-CatSystem. In this study, not only the

catalytic activity of COF-CNT was improved under the stimulation of an electric field, but also a new pathway was proposed for future smart therapy that can overcome the space-time limitation of the current therapies. In future research, we will further investigate the possibility of utilizing a self-generated electric field to provide energy to trigger catalytic reactions, change the reaction rates and thermodynamics, generate new intermediates, and change the interaction between substrates and nanocatalysts.

4. Experimental Section

Materials: 5,10,15,20-Tetrakis(4-aminophenyl)-21H,23H-porphine (TAPP), ferrous chloride (FeCl$_2$), DHPA, and multi-walled CNTs were acquired from Aladdin Reagent Co., Ltd. (Shanghai, China). Mesitylene, DBSA, anhydrous ethanol, acetic acid, 1,4-dioxane, tetrahydrofuran, and acetone were purchased from Shanghai McLin Biochemical Technology Co., Ltd. (Shanghai, China). TMB and PEDOT:PSS were obtained from Sigma-Aldrich Inc. (St. Louis, MO, USA). Calcein-acetoxymethyl ester (Calcein AM)/propidium iodide (PI) cell viability/cytotoxicity assay kit, 2,7-dichlorofluorescin diacetate, MMP assay kit with JC-1, bis-(1,3-dibutylbarbituric acid) trimethine oxonol (DiBAC4(3)), and 3-(4,5-dimethyl-2-Thiazolyl)-2,5-diphenyl tetrazolium bromide were purchased from Beijing Solab Technology Co., Ltd. (Beijing, China). Sheep blood samples were acquired from Beijing Land Bridge Technology Co., Ltd. (Beijing, China).

Preparation of PEDOT:PSS and PC: To synthesize PEDOT:PSS, a DBSA solution (4 v/v%) was added to PEDOT:PSS followed by agitation. Then, the mixture was poured into pre-patterned molds and centrifuged to remove the bubbles induced by vortex. PEDOT:PSS spontaneously formed within approximately 10 min[18]. COF-CNT was prepared according to

our previously reported method with slight modifications[17]. The detailed protocol is provided in the Supplementary Information. To synthesize PC, COF-CNT (1 mg mL^{-1}) was added to the PEDOT:PSS solution, and the subsequent procedure was the same as that employed for PEDOT:PSS.

Fabrication of TENG: To prepare the rectangular freestanding TENG, a Cu foil was attached to an acrylic substrate. Then, parts of the Cu foil were removed to form interdigital electrodes. For fabricating TENGs with different sizes, the gaps between adjacent electrodes were set to 1.13, 1.3, 1.35, 1.5 and 1.6 mm. A gap of 1 mm was maintained between adjacent electrodes to ensure electrical disconnection. The length and width of each Cu finger electrode were 3.3, 3.5, 3.9, 4.1, and 4.4 cm, and 3.3, 3.6, 3.9, 4.1, and 4.4 mm, respectively.

Measurement of the electrical output of the TENG: The V_{oc} and I_{sc} of the TENG were evaluated using a Keithley 6514 system electrometer.

Co-staining cells with Calcein-AM and PI: The cells in the PC group (the concentration of COF-CNT was 60 μg mL^{-1}) were incubated with PC in a transwell chamber (pore size: 0.4 μm) for 3 min, and then, Calcein-AM and PI were added. After being incubated for 30 min, the cells were washed twice with PBS. The cells in the PEDOT:PSS group were incubated with PEDOT:PSS in a transwell chamber for 3 min. Furthermore, the cells in the E, PEDOT:PSS+E, and PC+E groups were exposed to electric pulses for 3 min (3.5 Hz) with different materials in the transwell chambers. Fluorescence was observed using a confocal laser scanning microscope (CLSM) (Leica SP8).

Detection of intracellular ROS levels: 4T1 cells were seeded in a CLSM-exclusive culture disk (35 mm). Intracellular ROS levels of the cells after different treatments were determined

by detecting the fluorescence of 2,7-dichlorofluorescein (DCF) generated by the oxidation of DCFH-DA. The green fluorescence signal from DCF was analyzed via the CLSM.

Membrane potential measurement: To examine the effect of TENG electrical pulses on cell membrane potential, the cells after different treatments were incubated with DiBAC4(3) (5 µM in PBS) for 20 min. The TENG was used for electric field stimulation with the electric pulses of 3.5 Hz for a total time of 180 s. The change in green fluorescence was observed by the CLSM.

Measurement of MMP: The MMPs of the 4T1 cells after different treatments were measured by incubating the cells with 5 µg mL^{-1} JC-1 for 30 min. Fluorescence images were obtained using the CLSM.

Animals: BALB/c female mice aged ~6 weeks were provided by Beijing Charles River Laboratories, and the procedures for handling the animals were performed firmly according to the national standards "Laboratory Animal Requirements of Environment and Housing Facilities (GB 14925-2001)" The animal experiments were approved by the Biomedical Ethics Committee of Peking University (Approval Number: LA2019128).

In vivo cancer therapy: In vivo anticancer effects of TENG-CatSystem on the subcutaneous 4T1 tumors in BALB/c mice were investigated. 4T1 cells (5×10^5 cells suspended in 100 µL PBS) were injected into the subcutaneous area of the left lower abdomen of the mice. When the tumor volume reached ~100–200 mm^3, the mice were randomly divided into six groups (n = 6): 1) Control group: intratumoral injection of 100 µL PBS; 2) PEDOT:PSS group: intratumoral injection of 100 µL PEDOT:PSS; 3) E group: local injection of 100 µL PBS followed by electric field stimulation with TENG (3.5 Hz; 3 min); 4) PEDOT:PSS+E group: local injection of 100 µL PEDOT:PSS followed by electric field stimulation with TENG (3.5

Hz; 3 min); 5) PC group: local injection of 100 μL PC containing 1 mg mL^{-1} COF-CNT; and

6) PC+E group: local injection of 100 μL PC comprising 1 mg mL^{-1} COF-CNT followed by electric field stimulation with TENG (3.5 Hz; 3 min). Each mouse was earmarked and individually followed up throughout the experiment. Tumor volume and body weight were recorded until euthanasia. After 14 days of treatment, the mice were sacrificed, and the major organs and tumors were acquired for further pathological analysis by H&E staining and Ki-67 immunohistochemistry (for tumor tissues only). All the participants driving the TENG agreed with the experiment.

Statistical analysis: All data are expressed as mean ± s.d. error, n=4 and 6 for correspond to in vitro and in vivo experiments, respectively. Statistical differences between different groups of data were evaluated by one-way analysis of variance, and $p < 0.05$ was considered statistically significant. Asterisk (*) denotes statistical significance between bars (*$p < 0.05$, **$p < 0.01$, and ***$p < 0.001$) conducted using GraphPad Prism 6.0.

Date availability: The data that support the findings of this study are available from the corresponding author on reasonable request.

Supporting Information

Supporting Information is available from the Wiley Online Library or from the author.

Acknowledgements

References

[1]   a) I. Martinez-Reyes, N. S. Chandel, Nat Rev Cancer **2021**, 21, 669; b) I. Dagogo-Jack, A. T. Shaw, Nat Rev Clin Oncol **2018**, 15, 81.

[2]   a) S. F. Ji, B. Jiang, H. G. Hao, Y. J. Chen, J. C. Dong, Y. Mao, Z. D. Zhang, R. Gao, W. X. Chen, R. F. Zhang, Q. Liang, H. J. Li, S. H. Liu, Y. Wang, Q. H. Zhang, L. Gu, D. M. Duan, M. M. Liang, D. S. Wang, X. Y. Yan, Y. D. Li, Nature Catalysis **2021**, 4, 407; b) M. Liang, X. Yan, Acc Chem Res **2019**, 52, 2190.

[3]   H. Wang, Z. Gao, X. Liu, P. Agarwal, S. Zhao, D. W. Conroy, G. Ji, J. Yu, C. P. Jaroniec, Z. Liu, X. Lu, X. Li, X. He, Nat Commun **2018**, 9, 562.

[4]   a) Z. Lian, M. Sakamoto, H. Matsunaga, J. J. M. Vequizo, A. Yamakata, M. Haruta, H. Kurata, W. Ota, T. Sato, T. Teranishi, Nat Commun **2018**, 9, 2314; b) Y. Jiang, X. Zhao, J. Huang, J. Li, P. K. Upputuri, H. Sun, X. Han, M. Pramanik, Y. Miao, H. Duan, K. Pu, R. Zhang, Nat Commun **2020**, 11, 1857; c) J. Li, J. Huang, Y. Lyu, J. Huang, Y. Jiang, C. Xie, K. Pu, J Am Chem Soc **2019**, 141, 4073.

[5]   a) P. Zhu, Y. Chen, J. Shi, Adv Mater **2020**, 32, e2001976; b) K. Ma, G. Qi, B. Wang, T. Yu, Y. Zhang, H. Li, S. A. Kitte, Y. Jin, Nano Energy **2021**, 87, 106208.

[6]   M. Ge, D. Xu, Z. Chen, C. Wei, Y. Zhang, C. Yang, Y. Chen, H. Lin, J. Shi, Nano Lett **2021**, 21, 6764.

[7]   X. Ma, X. Ren, X. Guo, C. Fu, Q. Wu, L. Tan, H. Li, W. Zhang, X. Chen, H. Zhong, X. Meng, Biomaterials **2019**, 214, 119223.

[8]   a) T. Gu, Y. Wang, Y. Lu, L. Cheng, L. Feng, H. Zhang, X. Li, G. Han, Z. Liu, Adv Mater **2019**, 31, e1806803; b) T. Chen, T. Gu, L. Cheng, X. Li, G. Han, Z. Liu, Biomaterials **2020**, 255, 120202.

[9]   a) A. Warshel, Proc Natl Acad Sci U S A **1978**, 75, 5250; b) A. Warshel, P. K. Sharma, M. Kato, Y. Xiang, H. Liu, M. H. Olsson, Chem Rev **2006**, 106, 3210; c) R. C. Fear, S. E. Milan, R. Maggiolo, A. N. Fazakerley, I. Dandouras, S. B. Mende, Science **2014**, 346, 1506.

[10] S. Shaik, D. Mandal, R. Ramanan, Nat Chem **2016**, 8, 1091.

[11] D. Bim, A. N. Alexandrova, ACS Catal **2021**, 11, 6534.

[12] F.-R. Fan, Z.-Q. Tian, Z. Lin Wang, Nano Energy **2012**, 1, 328.

[13] Y. Song, J. Min, Y. Yu, H. Wang, Y. Yang, H. Zhang, W. Gao, Sci Adv **2020**, 6.

[14] a) Z. Liu, X. Liang, H. Liu, Z. Wang, T. Jiang, Y. Cheng, M. Wu, D. Xiang, Z. Li, Z. L. Wang, L. Li, ACS Nano **2020**, 14, 15458; b) Z. Liu, J. Nie, B. Miao, J. Li, Y. Cui, S. Wang, X. Zhang, G. Zhao, Y. Deng, Y. Wu, Z. Li, L. Li, Z. L. Wang, Adv Mater **2019**, 31, e1807795.

[15] S. Du, N. Zhou, G. Xie, Y. Chen, H. Suo, J. Xu, J. Tao, L. Zhang, J. Zhu, Nano Energy **2021**, 85, 106004.

[16] a) Y. Zhang, M. Xie, V. Adamaki, H. Khanbareh, C. R. Bowen, Chem Soc Rev **2017**, 46, 7757; b) Y. Chen, M. Wang, M. Tian, Y. Zhu, X. Wei, T. Jiang, S. Gao, Nano Energy **2017**, 42, 314.

[17] S. Yao, X. Zhao, X. Wan, X. Wang, T. Huang, J. Zhang, L. Li, Mater Horiz **2021**.

[18] S. Zhang, Y. Chen, H. Liu, Z. Wang, H. Ling, C. Wang, J. Ni, B. Celebi-Saltik, X. Wang, X. Meng, H. J. Kim, A. Baidya, S. Ahadian, N. Ashammakhi, M. R. Dokmeci, J. Travas-Sejdic, A. Khademhosseini, Adv Mater **2020**, 32, e1904752.

[19] a) Z. Chen, Z. Cai, C. Zhu, X. Song, Y. Qin, M. Zhu, T. Zhang, W. Cui, H. Tang, H. Zheng, Adv Healthc Mater **2020**, 9, e2001032; b) J. Wen, J. Tang, H. Ning, N. Hu, Y. Zhu, Y. Gong, C. Xu, Q. Zhao, X. Jiang, X. Hu, L. Lei, D. Wu, T. Huang, Advanced Functional Materials **2021**, 31, 2011176.

[20] X. Ding, G. Li, P. Zhang, E. Jin, C. Xiao, X. Chen, Advanced Functional Materials **2021**, 31, 2011230.

[21] S. Lin, C. S. Diercks, Y. B. Zhang, N. Kornienko, E. M. Nichols, Y. Zhao, A. R. Paris, D. Kim, P. Yang, O. M. Yaghi, C. J. Chang, Science **2015**, 349, 1208.

[22] G. Li, W. Hu, Y. Sun, J. Xu, X. Cai, X. Cheng, Y. Zhang, A. Tang, X. Liu, M. Chen, W. Ding, Y. Zhu, Angew Chem Int Ed Engl **2020**, 59, 21135.
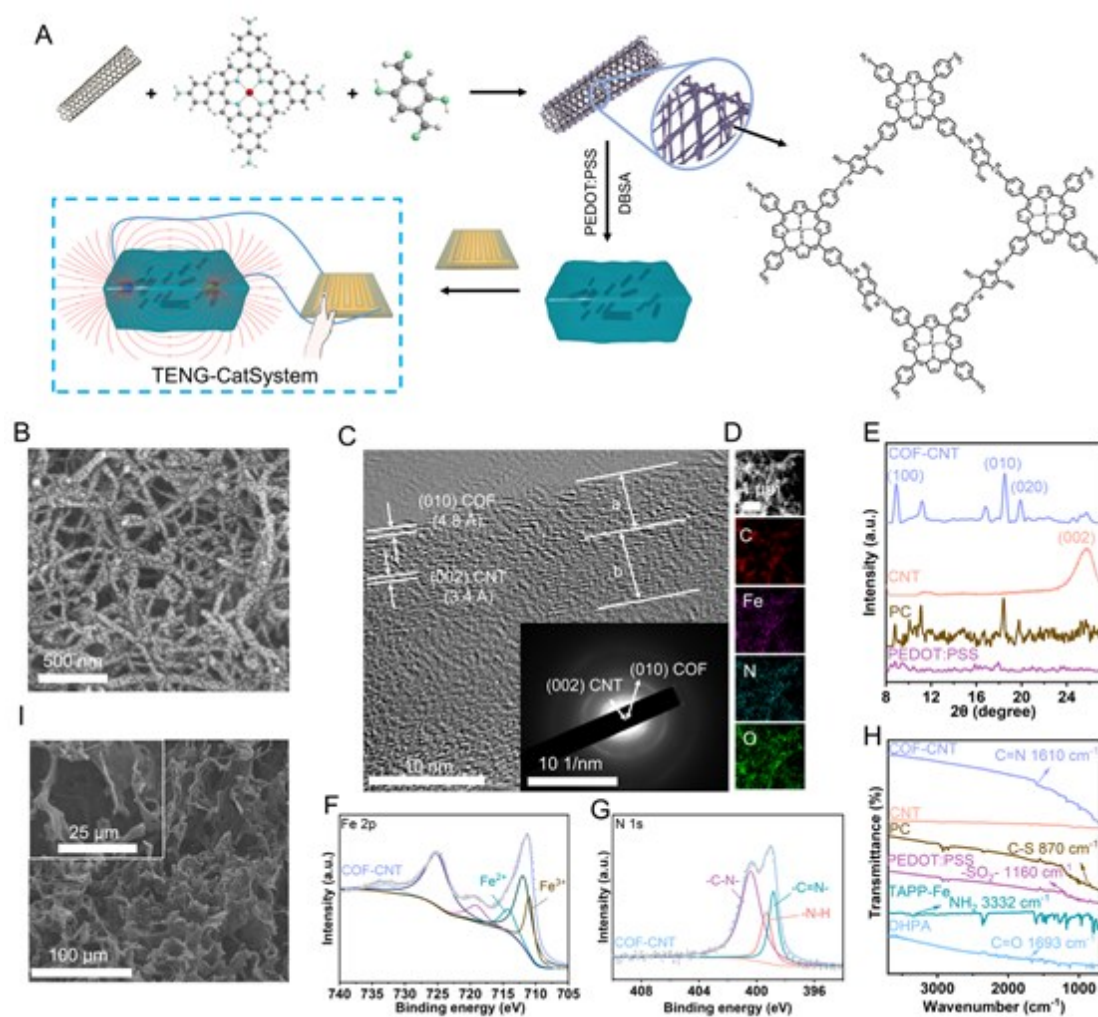
Figure 1. Preparation diagram and characterizations of COF-CNT and PC hydrogel. A) Schematic representation of preparing COF-CNT. B) SEM image. C) HRTEM image. The inset shows the diffraction rings of COF-CNT. D) Dark-field TEM image and corresponding energy dispersive spectroscopy (EDS) element mapping of COF-CNT: C (red), Fe (violet), N (blue), and O (green). E) XRD patterns of COF-CNT, PEDOT:PSS, CNT, and PC hydrogel. F) high-resolution Fe 2p XPS spectrum of COF-CNT. G) High-resolution N 1s XPS spectra of COF-CNT. H) FT-IR spectra of COF-CNT, CNT, PC hydrogel, PEDOT:PSS hydrogel, TAPP-Fe, and DHPA. I) SEM image of PC hydrogel.
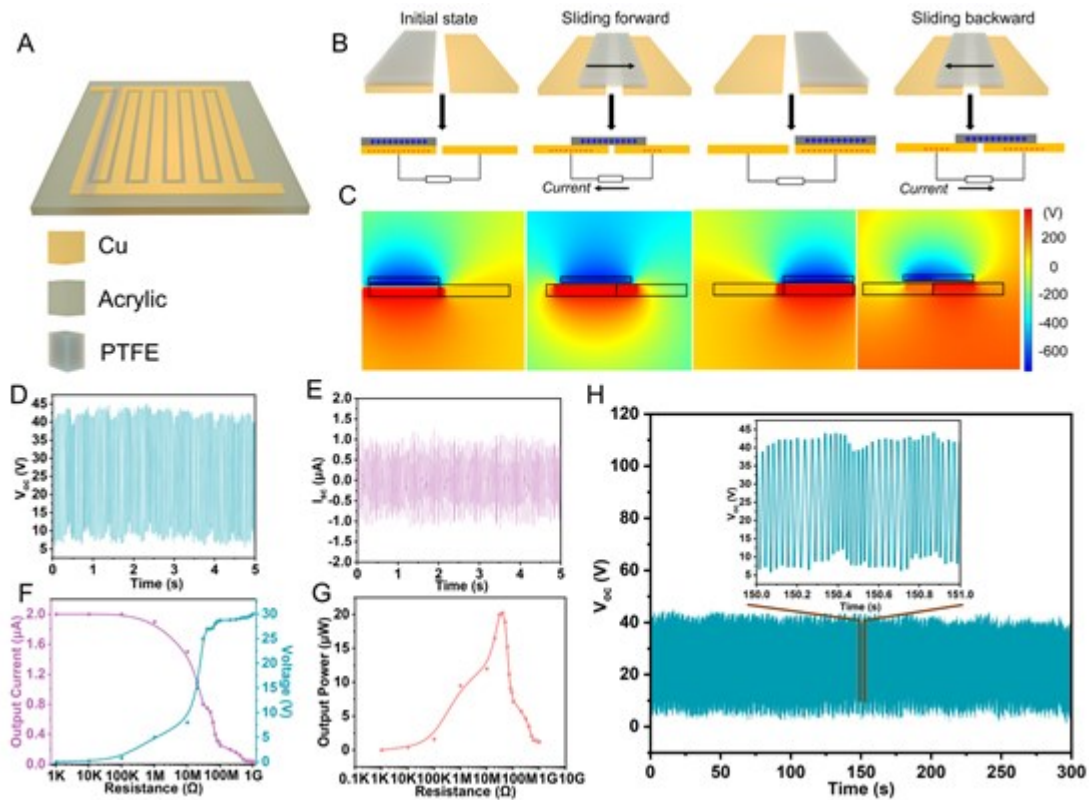
Figure 2. Fabrication and output performance of the IDE-based TENG. A) Schematic fabrication of the TENG. B) A cycle of electricity generation process of the TENG. C) Finite element simulation via COMSOL for analyzing the potential distribution during friction. (D) V_{oc} and (E) I_{sc} of the TENG within 5 s. F) The output current and voltage with the resistance of external loads. G) The output power with the resistance of the external loads. H) V_{oc} output stability of the TENG within 300 seconds. Inset shows the V_{oc} output within 1 s.
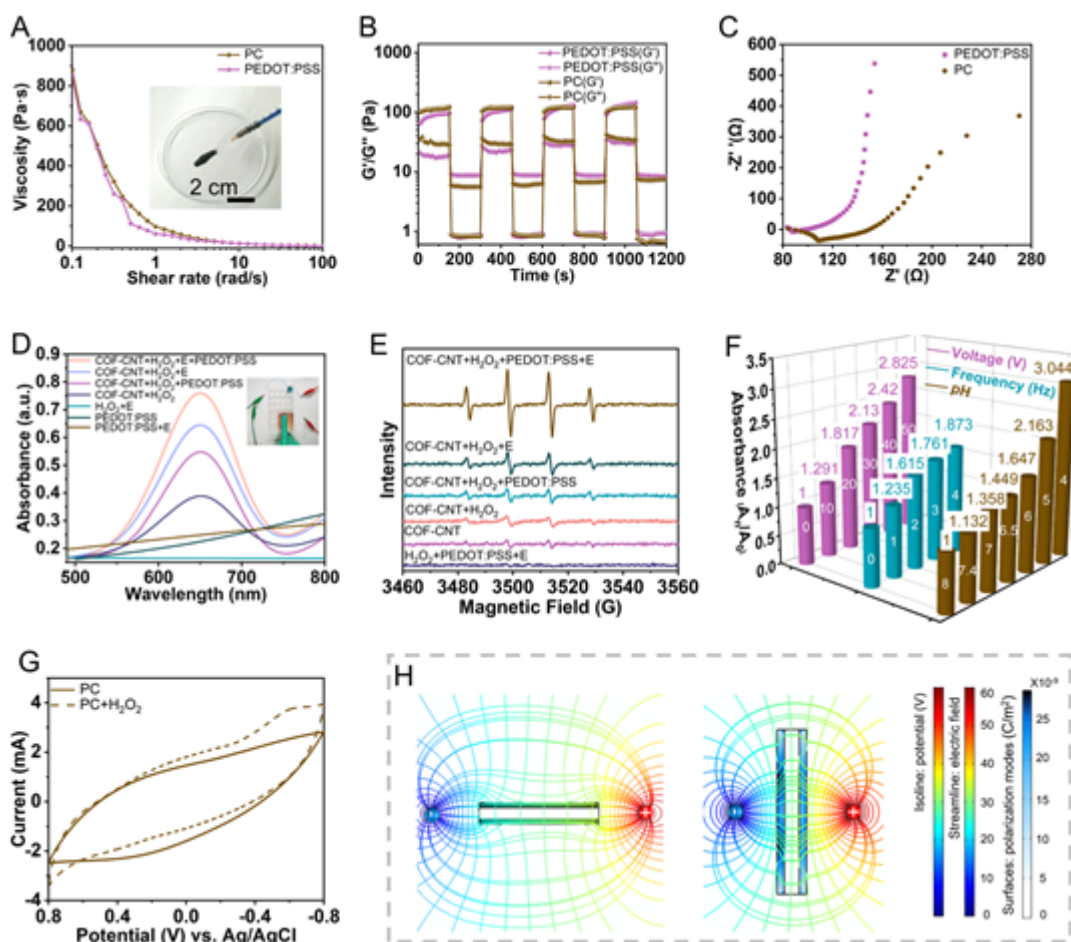
Figure 3. Mechanical and catalysis property. A) Viscosity of the PC at a shear rate of 0.1 to 100 s^{-1}. The inset shows the injectability of the hydrogel. B) Self-healing ability of the PC evaluated with an alternating strain of 1% and 100% at room temperature. C) EIS Nyquist plots for PEDOT:PSS and PC. D) POD-like activity of PC+E, PC, COF-CNT+E, COF-CNT, E, and PEDOT:PSS in pH 6.5 PBS with the addition of H_2O_2 (100 μM). The concentration of COF-CNT was 60 μg mL^{-1}. E) ESR spectra showing ·OH generation of COF-CNT+PEDOT:PSS, COF-CNT, and PEDOT:PSS with or without electric field and H2O2 (100 μM) using DMPO as the trapping agent. F) POD-like activities of PC (60 μg mL^{-1} COF-CNT) with 100 μM H_2O_2 at different pH (4, 5, 6, 6.5, 7, 7.4, and 8), TENG voltages (0, 10, 20, 30, 40 and 50 V) and frequencies (0, 1, 2, 3, and 4 Hz). G) Cyclic voltammograms of PC with and without H_2O_2. The medium was pH 6.5 PBS of 0.2 M. H) The schematic of the electric field distribution, potential distribution, and polarization mode distribution on the surface of the nanozymes, under the electricity of 30 V. Electric is shortened as E in some diagrams due to limited space.
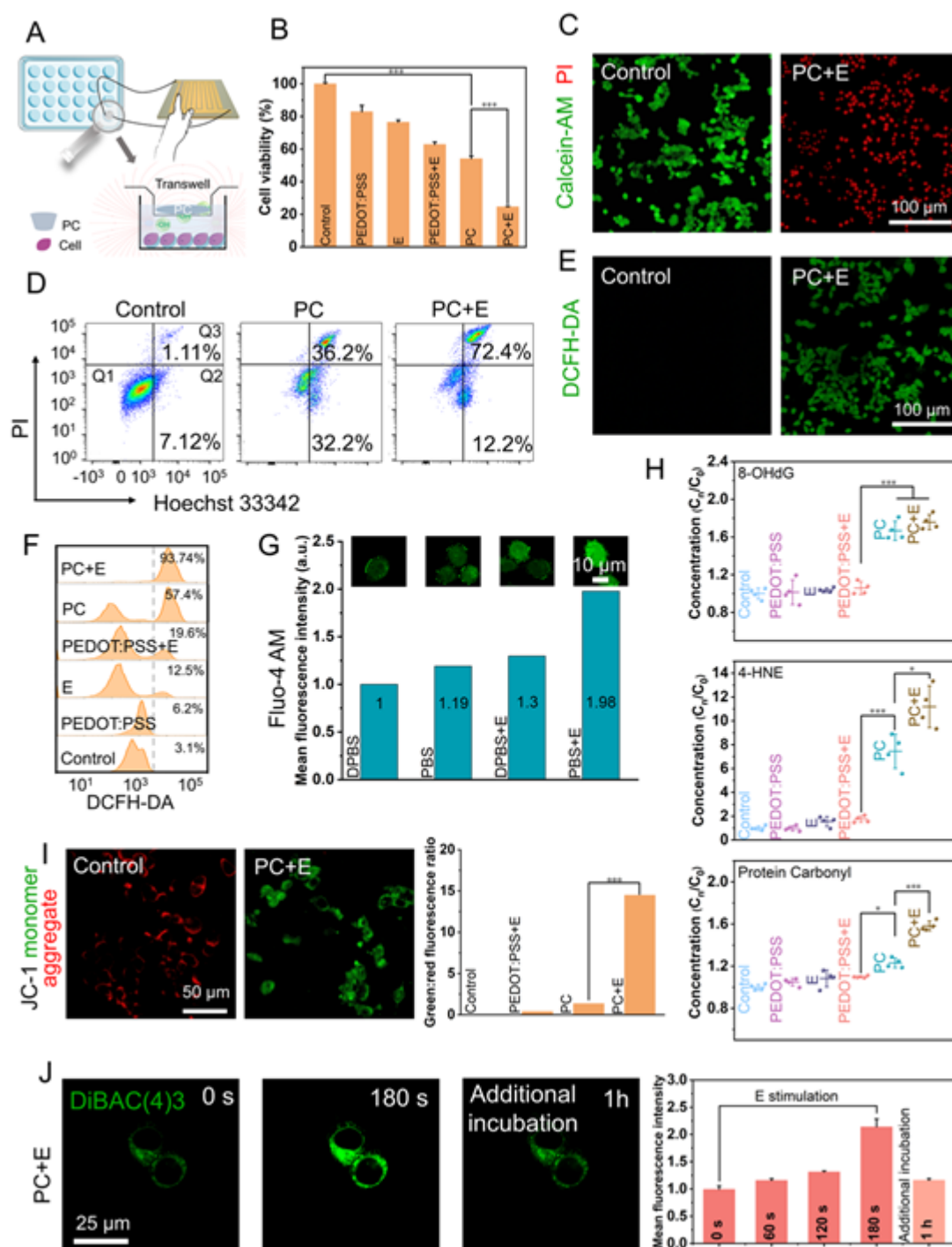
Figure 4. In vitro cancer therapeutic effect of the TENG-CatSystem. A) Schematic illustration of the TENG-promoted PC catalytic therapy in vitro. B) Cell viability of the 4T1 cells incubated with PBS, PEDOT:PSS, and PC with or without electric field stimulation (n=4). C) The 4T1 cells co-stained with Calcein-AM and PI and corresponding statistic result of dead cells. D) The flow cytometry analysis of cell apoptosis treated with PEDOT:PSS+E and PC+E. E) The 4T1 cells stained by DCFH-DA and the relative intensity of fluorescence

under different treatments. F) The flow cytometry analysis of 4T1 cells treated with PEDOT:PSS+E and PC+E to detect •OH generation. G) The 4T1 cells stained with Fluo-4 AM and the relative intensity of fluorescence after different treatments. H) Changes in 8-hydroxy-20-deoxyguanosine (8-OHdG), protein carbonyl (PCO), and 4-hydroxynonenal (4-HNE) content after different treatments (n=4). I) Confocal images showing JC-1 assay of the 4T1 cells treated with PEDOT:PSS and PC with or without the electric field stimulation. The statistic result shows the green:red fluorescence ratio under the different treatments. J) Fluorescence images and corresponding statistic results showing the plasma membrane potential change during and after the electric field stimulation for different time intervals. The cells were stained by DiBAC(4)3 (n=4). Statistical differences between different groups of data were evaluated by one-way analysis of variance, and $p < 0.05$ was considered statistically significant. Asterisk (*) denotes statistical significance between bars (*$p < 0.05$ and ***$p < 0.001$) conducted using GraphPad Prism 6.0.
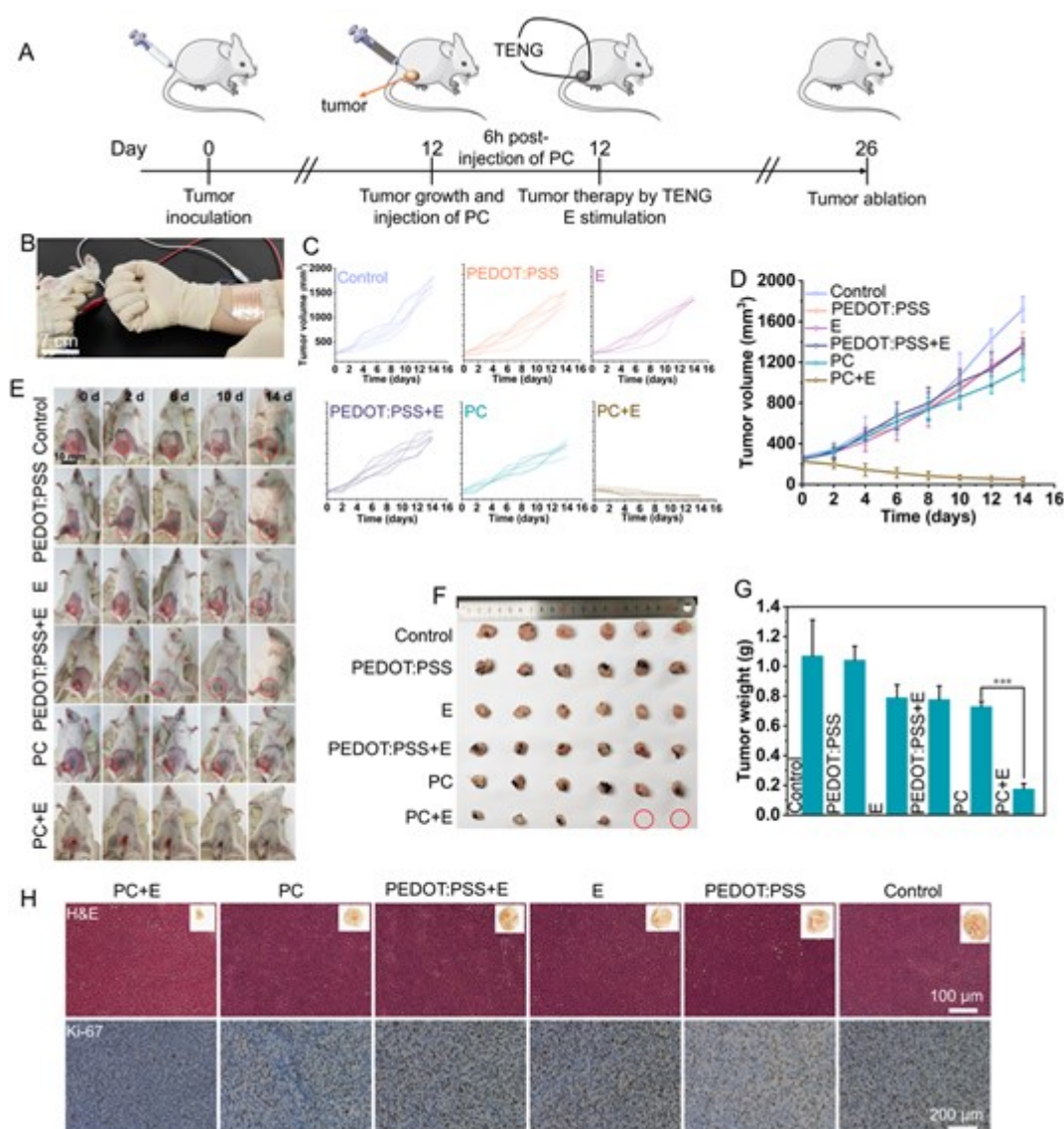
Figure 5. In vivo cancer therapy on the subcutaneous 4T1 tumor-bearing BALB/c mice. A) Schematic illustration of the cancer therapy with the self-driven TENG-CatSystem. B) Schematic illustration of the TENG promoted catalytic therapy in vivo. C-D) Tumor volume change of the mice during the treatment (n=6). E) Photos of the representative mice in different groups during the 14-days of treatment. F) Photos of the representative stripped tumor tissues at the terminal of the therapy. G) Mean tumor weights after the excision at day 14 (n=6). H) H&E and Ki-67 staining of the tumor tissues. Statistical differences between different groups of data were evaluated by one-way analysis of variance, and $p < 0.05$ was considered statistically significant. Asterisk (*) denotes statistical significance between bars (***$p < 0.001$) conducted using GraphPad Prism 6.0.

This work designed a human self-generated electric field-promoted system for improving cancer catalytic therapy. The human self-generated electric field increased the peroxidase-like activity of covalent organic framework nanozyme by about 4 folds to produce hydroxyl radical for efficient cancer therapy.

Shuncheng Yao, Xinyang Zhao, Xueyu Wang, Tian Huang, Yiming Ding, Jiaming Zhang, Zeyu Zhang, Zhong Lin Wang[*], Linlin Li[*]

Bioinspired Electron Polarization of Nanozyme with Human Self-Generated Electric Field for Cancer Catalytic Therapy